Batteries & Supercaps

Research Article
doi.org/10.1002/batt.202100305

Chemistry
Europe
European Chemical
Societies Publishing

www.batteries-supercaps.org

Investigation of the Anode-Electrolyte Interface in a Magnesium Full-Cell with Fluorinated Alkoxyborate-Based Electrolyte

Ananyo Roy,[a] Vinayan Bhagavathi Parambath,[a] Thomas Diemant,[a, c] Gregor Neusser,[d] Christine Kranz,[d] R. Jürgen Behm,[a, c] Zhenyou Li,*[a] Zhirong Zhao-Karger,[a, b] and Maximilian Fichtner[a, b]

Magnesium (Mg) anode-electrolyte interaction is not trivial and investigation of the interfacial process can be helpful for the development of Mg batteries. In this work, we studied the Mg metal anode cycled in a chloride (Cl)-free magnesium tetrakis (hexafluoroisopropyloxy) borate electrolyte using a full-cell configuration with TiS_2 model cathode. Electrochemical measurements and structural analysis of the cathode showed reversible de-/magnesiation of TiS_2 with some entrapment of irreversibly bound Mg^{2+}. Electrochemical impedance spectroscopy (EIS) was applied to analyze the Mg-electrolyte interaction in a three-electrode system. The results showed a rapid increase in charge transfer resistance on the anode side with increasing resting time. In contrast, we observed a significant drop in the charge transfer impedance upon cycling along with the appearance of an additional semi-circle, which suggested to the development of a solid interphase. X-ray photoelectron spectroscopy (XPS) and Fourier transform infrared spectroscopy (FTIR) corroborated the EIS results and confirmed the solid interphase layer formation, in which MgF_2 was identified as the primary species contributing to its formation. The current study provides fundamental insights into the interfacial phenomena between the metallic Mg anode and Cl-free electrolyte by highlighting the role played by the formed interphase on the reversible Mg stripping and plating in a Mg full-cell.

Introduction

Lower dendritic tendencies shown by Mg deposits in non-aqueous electrolytes ensure the safe incorporation of high capacity Mg metal as the anode.[1,2] As a consequence, rechargeable Mg batteries (RMBs) could potentially become a cheap and sustainable option for high energy density applications.[3] The breakthrough work by Aurbach et al.,[4] developing the first ever prototype RMB system and the continued progress being made with the magnesium sulfur-based conversion systems[5–7] underlines the genuine possibility of RMBs being an alternative or a complement to the already established Li-ion battery (LIBs) technology.

However, utilization of a metallic Mg anode in RMBs is problematic. Due to their low reduction potential (-2.37 V vs. SHE), metallic Mg anodes get easily passivated in polar aprotic electrolyte solutions, preventing further Mg-ion transport.[8,9] Only ether-based electrolytes have been reported to be compatible with Mg anodes. However, conventional Mg salts show low ionic conductivity in ether-based electrolytes.[10] Effective Mg dissolution in the electrolyte can be realized by either using strongly coordinating anions such as Cl^- to form complex ions[4,11] or by employing bulky anions which have lower association strength than the solvent molecules.[12–16] Compared to the Cl^- containing electrolytes, Mg salts with weakly coordinating anions typically possess a higher chemical stability and provide a wider electrochemical window. Hence, they can be considered as a more viable option to overcome the electrolyte related challenges in RMB systems.[17,18]

Mg cells with both Cl-based and Cl-free electrolytes have already shown long-term reversible Mg stripping/plating.[5,19] In case of Cl-based electrolytes, Cl-ions are preferentially adsorbed on the anode surface and play a decisive role for the interfacial charge transfer, enabling stable cycling.[10,20] Another report indicated the formation of an intermediate layer comprised of soluble complex $[MgCl \cdot 5THF]^+$.[21] In contrast, the Mg plating/stripping performance in a Cl-free electrolyte presumably results from a different interfacial phenomena.[22,23] Previous symmetric-cell studies with a Cl-free electrolyte also identified an adsorption layer, which was claimed to result from an

[a] A. Roy, Dr. V. Bhagavathi Parambath, Dr. T. Diemant, Prof. R. J. Behm, Dr. Z. Li, Dr. Z. Zhao-Karger, Prof. M. Fichtner
Helmholtz Institute Ulm (HIU) Electrochemical Energy Storage, Helmholtzstraße 11, 89081 Ulm, Germany
E-mail: zhenyou.li@kit.edu

[b] Dr. Z. Zhao-Karger, Prof. M. Fichtner
Institute of Nanotechnology (INT), Karlsruhe Institute of Technology (KIT), P. O. Box 3640, 76021 Karlsruhe, Germany

[c] Dr. T. Diemant, Prof. R. J. Behm
Institute of Surface Chemistry and Catalysis, Ulm University, Albert-Einstein-Allee 47, 89081 Ulm, Germany

[d] Dr. G. Neusser, Prof. C. Kranz
Institute of Analytical and Bioanalytical Chemistry, Ulm University, Albert-Einstein-Allee 11, 89081 Ulm, Germany

accumulation of electrochemically inactive species during resting periods.[5,24] However, this adsorption layer is dynamic and would be broken down once the cell is switched to an operational state.[5,22] Due to the sluggish solid diffusivity of Mg^{2+}, it was believed that a interphase-free anode is necessary for the electrochemical processes at anode side.[10,25] However, maintaining the reductive metallic Mg surface during continuous plating/stripping in organic electrolyte is questionable, particularly with the absence of Cl^-. Since the stability of interfaces and interphases is essential for a sustained cell operation, the physical reasons and conditions for a highly reversible Mg cycling in Cl-free electrolytes still need to be explored.

In this work, we have tried to clarify these issues by studying the anode-electrolyte interphase formation and its influence on the electrochemical performance under the practical environment of a RMB full-cell model system. The model system consisted of an intercalation-type TiS_2 cathode, Cl-free magnesium tetrakis(hexafluoroisopropyloxy)borate electrolyte dissolved in dimethoxyethane ($Mg[B(hfip)_4]_2$/DME)[15] and a metallic Mg anode. TiS_2, which in fact was the first cathode material used for Li^+ insertion,[26] has a well-defined layered structure and the presence of "softer" sulfur atoms make it more suitable for Mg^{2+} intercalation than oxides.[27] Reversible insertion of Mg^{2+} ions into TiS_2 has been characterized by ex situ X-ray diffraction (XRD) and operando Raman spectroscopy. Anode-electrolyte interfacial phenomena, such as the formation of an adsorption layer and a solid interphase layer under static and dynamic operational conditions, respectively, were monitored and characterized by a combined electrochemical and spectroscopic analysis. Finally, we established correlations between the electrochemical results and the processes occurring at the anode-electrolyte interface, which demonstrated that interfacial phenomena plays an important role on the RMB performance during the initial cycles.

Results and Discussion

Establishment and validation of the RMB model system

The motivation behind employing a full-cell RMB as model system was to study the effect of the anode-electrolyte interaction in a practical system. The full-cell was built by coupling a nanostructured TiS_2 cathode with a Mg anode and using 0.3 M $Mg[B(hfip)_4]_2$/DME as the electrolyte. Submicron TiS_2 particles were obtained by ball-milling the commercial micrometer-sized TiS_2 powder to improve the reversible Mg storage capability. Comparison of SEM images before and after ball-milling (Figure S1a and b) reveals a reduction of the mean particle size from more than 1 μm to below 1 μm upon milling. Mechanical milling greatly improves the de-/insertion process and thus the electrochemical performance by shortening the diffusion path length of Mg^{2+}. On the other hand, however, ball-milling also leads to surface degradation and defect formation.[28] The XRD pattern of the ball-milled TiS_2, which shows the trigonal symmetry of a $P\bar{3}m1$ space group (Fig-

ure S2), agreed reasonably with the reference pattern PDF 00–015-0853, indicating that the main structural characteristics were maintained. The octahedral and tetrahedral voids illustrated in Figure 1(a) are the potential Mg^{2+} storage sites. Accommodation of 0.5 Mg^{2+} (1 e^- transfer) per TiS_2 formula unit gives a theoretical specific gravimetric capacity of 240 mAh g^{-1}. At a current density of 20 mA g^{-1} (C/12) and under ambient conditions, an initial discharge capacity of 100 mAh g^{-1} ($Mg_{0.2}TiS_2$) was delivered (Figure 1b), which is less than half of the theoretical value. The average Mg content measured by energy dispersive X-ray spectroscopy (EDX) after the first discharge was 0.2 ± 0.02 (Table 1), which agreed well with the obtained discharge capacity. The corresponding charging process resulted in a specific capacity of ~36.5 mAh g^{-1}. The considerable capacity deficit of ~63.5 mAh g^{-1} is very likely due to an incomplete extraction of Mg^{2+} from the TiS_2 cathode.[29] The EDX measurement of the fully charged sample showed that 0.15 ± 0.02 Mg^{2+} was still present in the cathode. This confirms the significant trapping of Mg^{2+} during the first cycle and accounts for the substantial capacity loss observed in the second cycle. Nonetheless, a stable specific discharge capacity of 50 mAh g^{-1} was delivered from the 30th cycle onwards (Figure 1d). The low Coulombic efficiency might indicate side reactions at high voltages and needs to be investigated further. The rate capability (Figure S3) of the ball milled TiS_2 delivered capacities of ~45 mAh g^{-1}, ~40 mAh g^{-1} at current densities of 60 mA g^{-1} (C/4) and 120 mA g^{-1} (C/2) respectively. The capacity dropped further to ~32 mAh g^{-1} at 240 mA g^{-1} (1 C) and to ~25 mAh g^{-1} when cycled at 480 mA g^{-1} (2 C).

To cross-check the galvanostatic data above, three-electrode (PAT CELL core from EL CELL®) electrochemical measurements were conducted to decouple the contributions of anode and cathode on the full-cell performance. The corresponding three-electrode cyclic voltammogram (Figure 1c) shows quite broad redox peaks, which points to a slow Mg^{2+} diffusion in the TiS_2 lattice. Based on the broad reduction peak around 1.0 V vs. Mg_{ref} in the first cycle, reversible Mg^{2+} insertion takes place around that potential. In addition, there is also a small reduction peak at 1.7 V, whose identity is unclear so far. One possibility could be the conversion of S residues, which were most likely generated during ball-milling. Theoretically, Mg–S conversion redox reaction occurs at a potential of 1.77 V.[5] However, no corresponding oxidation peak was observed and the reduction peak decreased in intensity rapidly after the second cycle and completely disappeared by the fifth cycle. Thus, indicating that an irreversible process occurred at 1.7 V. Hence, an alternative explanation could be that this peak is related to the irreversible Mg^{2+} entrapment after the first cycle, possibly due to local structural modifications, which results in the formation of a partially magnesiated Mg_xTiS_2 ($x \sim 0.15$)phase

Table 1. Stoichiometry of layered TiS_2 determined by EDX.

sample	pristine	1st discharge	1st charge
stoichiometry	$Ti_{0.85}S_2$	$Mg_{0.2}Ti_{0.85}S_2$	$Mg_{0.15}Ti_{0.81}S_2$

Batteries & Supercaps

Research Article
doi.org/10.1002/batt.202100305

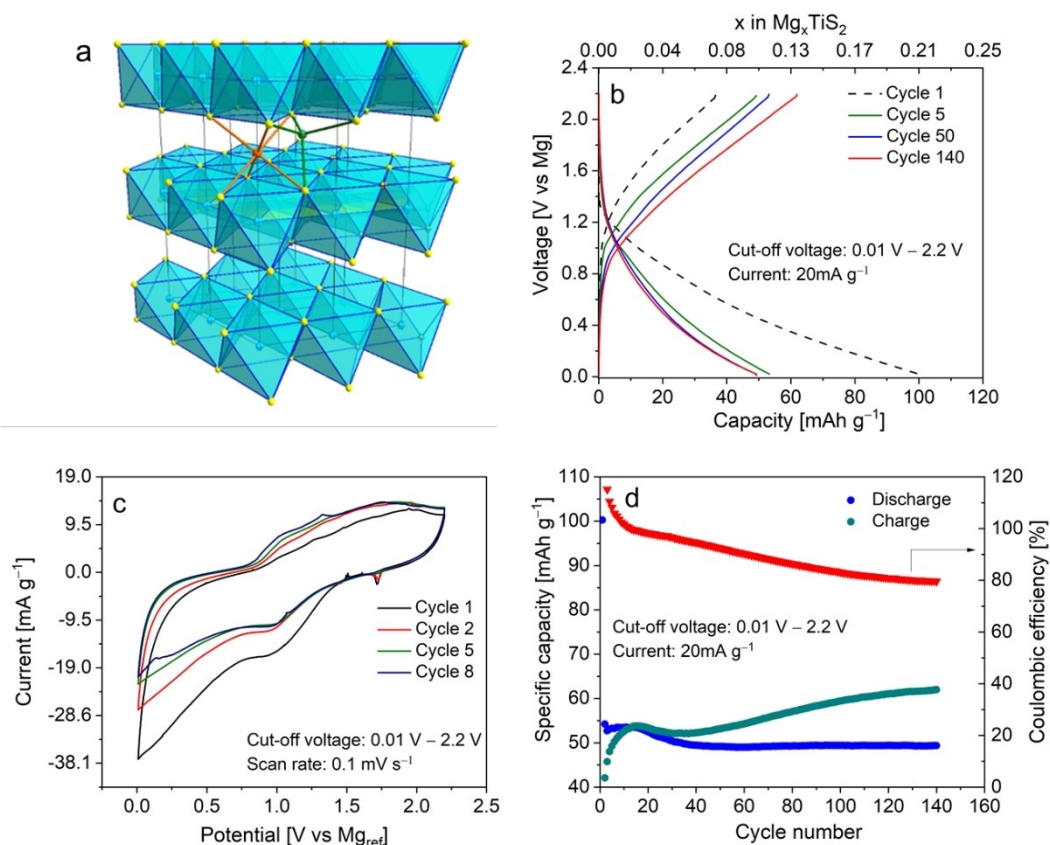**Chemistry Europe**
European Chemical
Societies Publishing

Figure 1. a) Crystal structure of TiS_2. Titanium atoms (blue) occupies the octahedral sites (blue) created by the sulfur (yellow) cage. The interlayer space has octahedral (orange) and tetrahedral (green) voids that can be occupied by Mg^{2+}. b) Charge and discharge voltage profile of TiS_2 against Mg anode at room temperature in the voltage range of 0.01–2.2 V (two electrode setup). c) Cyclic voltammogram of the full-cell with Mg reference (three electrode setup). d) Charge (green)/ discharge (blue) capacity and Coulombic efficiency (red) versus cycle number.

with some irreversibly blocked sites, presumed to be the octahedral void sites.[29] The eventual stabilization of the current and capacity in Figure 1(c and d) respectively after the first cycle indicates steady and reversible de-/insertion of Mg^{2+} from the second cycle onwards and agrees nicely with the two-electrode galvanostatic data.

Post-mortem XRD: To have a closer look into the structural evolution after de-/magnesiation, ex-situ XRD measurements were conducted on TiS_2 electrodes after the first discharge and charge steps respectively, as shown in Figure 2(a). After the first full discharge, it was observed that the diffraction peaks ostensibly did not shift but underwent reasonable broadening
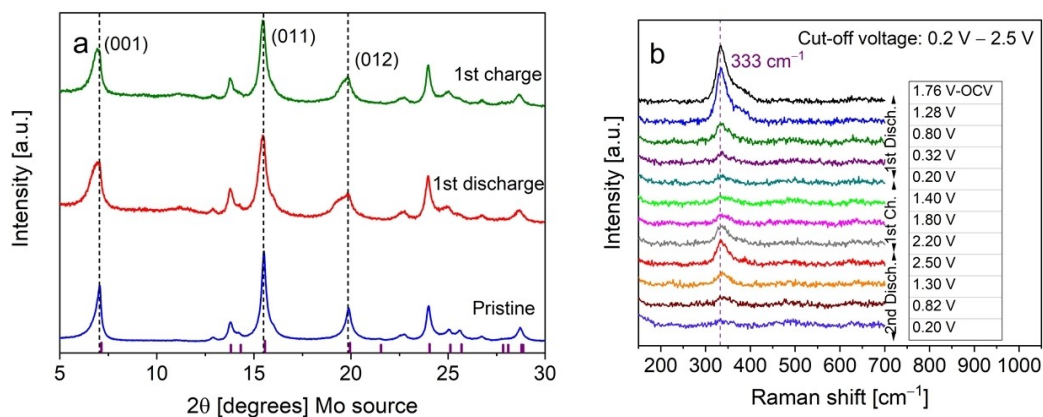

Figure 2. a) Post mortem XRD pattern of the discharged (red), charged (green) and pristine (blue) TiS_2 cathode after running 1 complete cycle at a current of $5\ mA\,g^{-1}$. b) In-situ Raman spectra of the TiS_2 cathode with the cell operated in the voltage range of 0.2–2.5 V.

Batteries & Supercaps

Research Article
doi.org/10.1002/batt.202100305

**Chemistry
Europe**

European Chemical
Societies Publishing

compared to the pristine TiS_2. A likely reason behind the broadening could be that the peaks representing the partly magnesiated and pristine phases of TiS_2 were not clearly resolved on completion of the first full discharge with the smaller wavelength Mo source ($\lambda = 0.7092$ Å). In fact, according to a previous in-situ XRD study with Cu–K_α radiation ($\lambda = 1.54$ Å), the (001) peak showed clear splitted peaks on complete discharge. The split peaks were located at 14.5° (partly magnesiated phase) and 15.5° (existing pristine phase). With the Mo source, the corresponding peaks should be positioned close to one another at ~6.67° (partly magnesiated phase) and ~7.12° (existing pristine phase) according to Braggs' law. This agrees with the broad feature of the (001) peak, which is located in the 2θ range of 6.2°–7.35°. Also, on taking a closer look at the (012) diffraction peak (Figure 2a), it is quite clear that after the first discharge, a shoulder peak appears at ~19° which was not present for the pristine TiS_2 phase, indicating the formation of a magnesiated phase along with remnant pristine phase.

On charging, the broadening of the peaks reduced, but the sharp pristine profile was not recovered. This implies that Mg^{2+} was not completely extracted from the host structure as a result of irreversible trapping. Consequently, the pristine TiS_2 phase was not fully recovered. But nonetheless, the post mortem XRD indicates that reversible de-/insertion of Mg^{2+} is still possible in TiS_2 to some degree.

Operando Raman spectroscopy: The structural change was also visible in the respective operando Raman spectra of the ball-milled TiS_2 as shown in Figure 2(b). TiS_2 showed the prominent Raman active out-of-plane (A_{1g}) mode at 333 cm^{-1}, which is characteristic for the octahedral (1T) polymorph of pristine TiS_2 (Figure 2b). The cell was cycled between 0.2–2.5 V and the spectroscopic measurement was conducted at different states of charge (see Experimental Section for more details). At the open circuit voltage (OCV) condition (1.76 V), we noticed a prominent peak at 333 cm^{-1}, along with a shoulder at 368 cm^{-1}. This shoulder was possibly due to the creation of defects in TiS_2 as a result of the initial ball milling process that possibly led to an excess of interlayer metal atoms,[28] which in turn caused a stiffening of the phonon modes. As more Mg^{2+} was intercalated into TiS_2 lattice, the peak at 333 cm^{-1} decreased in intensity, appeared broadened and merged with the peak at 368 cm^{-1}. The gradual decrease in the intensity of the A_{1g} mode during discharge is possibly due to the formation of a magnesiated phase (Mg_xTiS_2) and the associated large distortions in the TiS_2 lattice.[30] Furthermore, the change in the overall profile of the A_{1g} peak indicates that the surrounding chemical environment had changed with the intercalation of Mg^{2+}.

The following charging process led to the re-appearance of the A_{1g} vibration mode, indicative of reversible de-/magnesiation, but the intensity is significantly less than that of pristine TiS_2. This clearly shows the limited reversibility of the de-/magnesiation process and the onset of permanent structural distortion in the TiS_2 lattice, in good agreement with the ex-situ XRD data. This conclusion is also supported by the much lower intensity of the peak at 1.3 V during the second discharge as compared to the intensity of the peak at 1.28 V (Figure 2b) during the first discharge, respectively, due to irreversible Mg^{2+} entrapment. Nevertheless, the operando Raman data confirms a reasonable reversibility of Mg^{2+} de-/insertion for the ball-milled TiS_2 cathode, despite the limited mobility of the Mg-ions.

Investigation of the anode-electrolyte interface

In the established model system, we further investigated the anode-electrolyte interface by a combined electrochemical and spectroscopic approach. Particular efforts were made for examining the interaction of the $Mg[B(hfip)_4]_2$/DME electrolyte with the metallic Mg anode and possible interphase formation. In order to probe the anode-electrolyte interface, we performed EIS measurements in a three-electrode cell, both under rest at the OCV (before cycling) and after cycling (post-cycling condition). In the latter case an equilibration time of 10 min was added to stabilize the cell potential after each cycle. The Nyquist plot in Figure 3(a) shows that the charge transfer resistance at the anode after 1 h rest was 29 kΩ cm^2, while after
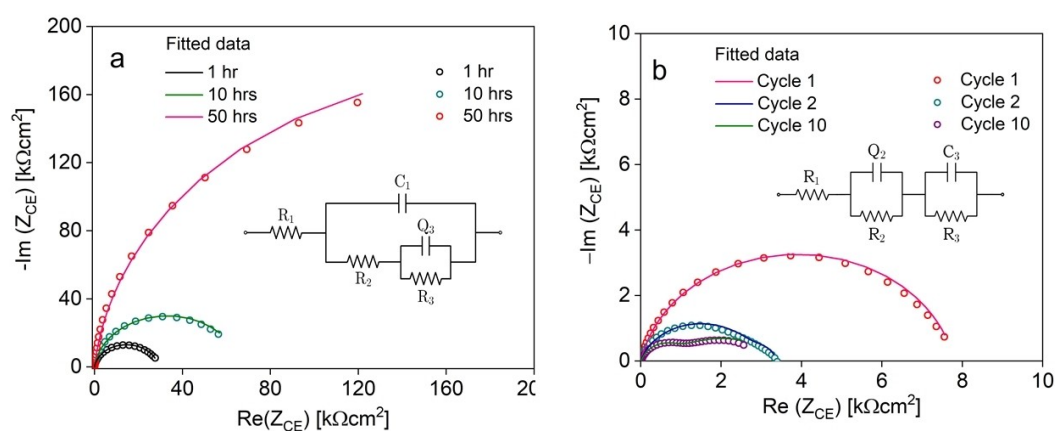

Figure 3. a) Impedance spectra from the anode side of the pre-cycled three-electrode cell. b) Impedance spectra from the anode side of the post-cycled three-electrode cell.

Batteries & Supercaps

Research Article
doi.org/10.1002/batt.202100305

**Chemistry
Europe**
European Chemical
Societies Publishing

10 h, it increased to 66 kΩ cm^2, and over 120 kΩ cm^2 after 50 h. Hence, with increasing rest time the charge transfer resistance increased significantly.

The measured data were modelled with the equivalent electrical circuit shown in the inset in Figure 3a,[31] where R_1 represents the bulk electrolyte resistance and R_3 corresponds to the charge transfer resistance. The electrical double layer (EDL) capacitance across the electrode-electrolyte interface is represented by the capacitive phase element (CPE) Q_3. The simulated results (Table S1) indicated the formation of an inhomogeneous and ionically non-conducting layer on the surface of the Mg anode, which is represented here by the finite resistive element R_2. The possibility of the layer being inhomogeneous was because the equivalent circuit that was used to fit the EIS measurement corresponded to such an inhomogeneous layer formation. This non-conducting layer had likely developed by adsorbing ionic clusters or solvent molecules during extended exposure of the Mg anode surface to the electrolyte as has been previously reported.[24]

The impedance data recorded under post-cycle condition (Figure 3b) illustrates the electrochemical interaction between Mg anode and the Mg[B(hfip)$_4$]$_2$/DME electrolyte, as demonstrated by the variation in the charge transfer resistance with increasing cycling. After the first cycle, charge transfer resistance dropped approximately to 7.7 kΩ cm^2, significantly lower than the charge transfer resistance of the pre-cycled cell. After completion of the 2nd cycle, it further decreased to 3.2 kΩ cm^2 and following the 10th cycle, the charge transfer resistance was reduced to 2.8 kΩ cm^2. The rapid drop in the charge transfer resistance occurs during the initial two cycles before eventually stabilizing. The corresponding time dependent voltage of the anode E_{CE} also showed a reduction of the overpotential during the initial cycles (Figure S4), in good agreement with the change in the impedance. Apparently, a stable interphase formed during the initial cycles, probably similar to the conducting solid-electrolyte interphase (SEI) reported extensively in the literature regarding LIBs.[32] The EIS spectra were

modelled with another equivalent electrical circuit, which is shown in Figure 3(b) (inset). It is composed of resistive elements R_1, R_2 and R_3 and capacitive elements Q_2 and C_3, where Q_2 is the CPE. R_1 represents the bulk electrolyte resistance. The resistive element R_2 is determined by the low frequency intercept of the Nyquist plot and corresponds to the charge transfer resistance. Q_2 simulates the effect of EDL capacitance, and the RC circuit element (R_3, C_3 in series) describes the formation of a solid interphase layer with finite resistance.

Focusing on the Nyquist plot recorded after the 10th cycle (Figure 3b), clearly resolves an additional semi-circle in the mid to low frequency regime. This was indicative of a new electro-chemical process, most likely related to the formation of a solid interphase layer. Since this is clearly visible after the 10th cycle, the development of the interphase obviously takes a few cycles. Another aspect of interest is that the value of the resistance R_3, corresponding to the solid interphase, increased with cycling (Table S2). This reflects an increase in the thickness of the formed layer on the Mg anode, which can be described by the relation $R = \rho L/A$, where ρ is the resistivity, L is the thickness and A is the surface area of the presumably freshly formed interphase. On the other hand, the impedance of the cathode (Figure S5a and b) demonstrated a very small charge transfer resistance compared to the impedance from the anode. Furthermore, the charge transfer resistance remained independent of both time and cycling index. This indicates that the charge transfer across the cathode-electrolyte interface was relatively easier compared to the charge transfer across the anode-electrolyte interface.

Post-mortem infrared spectroscopy: To obtain chemical information about the solid interphase, the surface of the Mg anode from the cycled full-cell was analysed with the help of attenuated internal reflection Fourier transform infrared spectroscopy or ATR-FTIR technique. Figure 4 compares the fingerprint regions of the IR spectrum of the pure Mg[B(hfip)$_4$]$_2$/DME electrolyte with the cycled Mg anode surface. The distinct
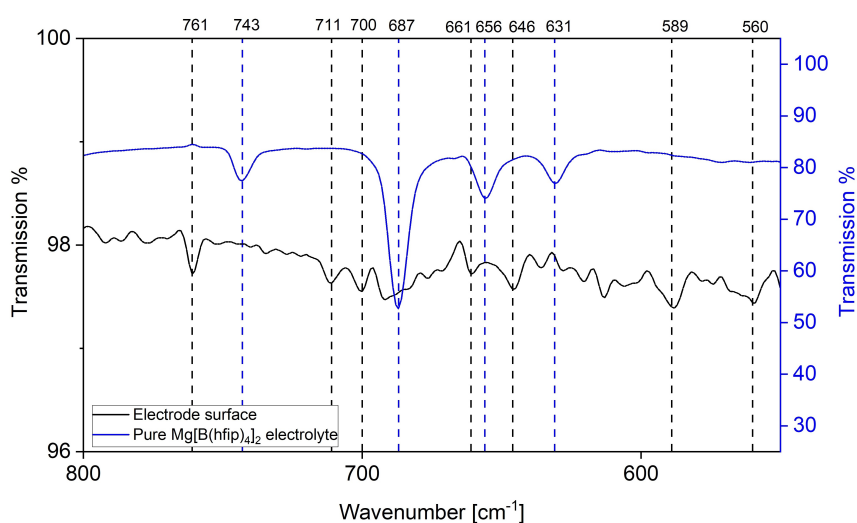

Figure 4. IR spectra of the pure Mg[B(hfip)$_4$]$_2$/DME salt and the Mg anode after 20 cycles.

Batteries & Supercaps

Research Article
doi.org/10.1002/batt.202100305

Chemistry Europe
European Chemical
Societies Publishing

bands from the electrolyte located at 743, 687, 656 and 631 cm^{-1} originate from the vibration of the carbon-fluorine bonds.[33] These bands also appear in the IR finger-print of the cycled Mg anode, but are slightly shifted towards higher wavenumbers, pointing to the deposition of electrolyte molecules on the Mg surface. The bands positioned at 711 and 700 cm^{-1} correspond to metal-fluorine stretch, possibly from the decomposition products of the fluorinated $Mg[B(hfip)_4]_2$/DME electrolyte. In addition, another band pair was observed at 589 and 560 cm^{-1}, which can be characterized as organometallic species but their specific identities are still not clear.[33] The assignment of all the bands are listed in Table S3.

X-ray photoelectron spectroscopy: In addition to the findings from IR spectroscopy, post mortem XPS measurements were also conducted on the Mg anode surface after 20 cycles. The survey spectrum in Figure S6(a) shows a prominent F1s peak at $\sim$688 eV, which was caused by the fluorinated $Mg[B-(hfip)_4]_2$/DME electrolyte and its decomposition products. A closer look into the detail spectrum in the F1s range (Figure 5a) reveals two prominent features at 688.6 and 685.2 eV, which can be assigned to organofluoride species (like $-CF_2$ and/or $-CF_3$) and to MgF_2, respectively. After removal of $\sim$3 nm of the top most surface by Ar$^+$ ion sputtering, it was noticed that the intensity of the MgF_2 peak increased substantially (Figure 5a). Further sputtering to depth of $\sim$10 nm (Figure 5a) showed a similar intensity ratio, thus indicating that the concentration of MgF_2 stabilized beneath the top layer of the interphase. The Mg 2p spectrum (Figure 5b) showed only one broad feature at $\sim$50.5 eV, which was due to various oxidized Mg species. In an effort to estimate the contribution of MgF_2 to this broad feature, a peak fit was carried out in which MgF_2 is represented by a peak at 51.0 eV while all other oxidized Mg species are subsumed in a peak in the range of 50.3–50.6 eV. The intensity of the peak related to MgF_2 was evaluated from the intensity of the F1s peak of MgF_2 taking into account the atomic sensitivity factors of the two peaks and the stoichiometry of MgF_2. Comparison of the results at different layer depths showed a significant increase of the MgF_2 contribution to the peak upon

sputtering; from 10% at the top most surface to $\sim$50% and $\sim$60% after removal of $\sim$3 and $\sim$10 nm of the surface layer. In addition, B1s peak was also observed (Figure S6b), most likely from the borate present in the electrolyte decomposition products. Since bulk MgF_2 is not a good ionic conductor and has large migration energy barrier for Mg^{2+},[34] the solid interphase is possibly porous, which allows the transport of Mg^{2+}. Another study regarding reversible Mg and Ca plating also reported such an interphase.[35,36] Finally, it may be noted that the feature of metallic Mg of the bulk electrode, which is expected to occur at $\sim$49 eV, was not detected even after the second sputtering step, indicating a relatively thick solid interphase layer. Moreover, compared to the study recently done by Li et al. on a cycled Mg anode from a Mg–Mg symmetric cell,[37] the solid interphase formed in the full-cell was thicker. A glance at Figure S7 also shows that the concentration of fluorine and boron increased with cumulative sputtering times, thus verifying that the solid interphase is composed of MgF_2 and boron-based species. Therefore, the XPS spectra reinforces the findings of the EIS and provides satisfactory chemical proof which confirms the formation of a solid interphase upon cycling that allows charge transfer at the anode-electrolyte interface while reducing the charge transfer resistance and thereby the overpotential. Moreover, the solid interphase also ensures an electrochemically stable interface on the anode side, thus enabling stable long-term cycling performance.

Scanning electron microscopy: To investigate the morphology of the anode-electrolyte interface, SEM images were recorded of the surface of the Mg anode after 20 cycles and was compared with that of a pristine (polished) sample. The surface morphology of the cycled Mg anode, shown in Figure 6(a), appeared porous compared to the pristine sample (Figure 6b). Additionally, it consisted of many small spherical particles, presumably Mg nano particles. Despite the general unevenness of the surface, no significant sharp growths resembling dendrites were observed. The diameters of the spherical particles ranged approximately between 10 and
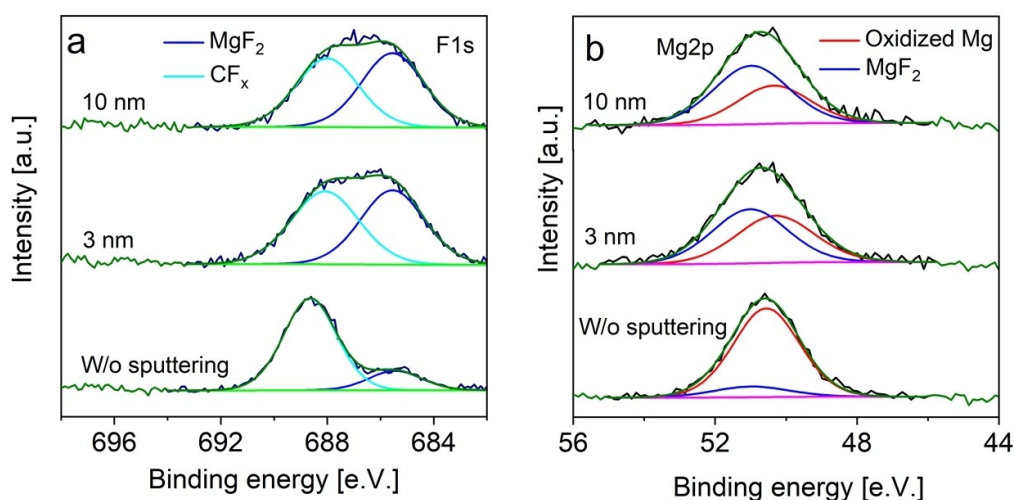
Figure 5. a) XPS spectra of F1s at different sputtered depths. b) XPS spectra of Mg2p after different sputtering times.

Batteries & Supercaps

Research Article
doi.org/10.1002/batt.202100305

Chemistry Europe
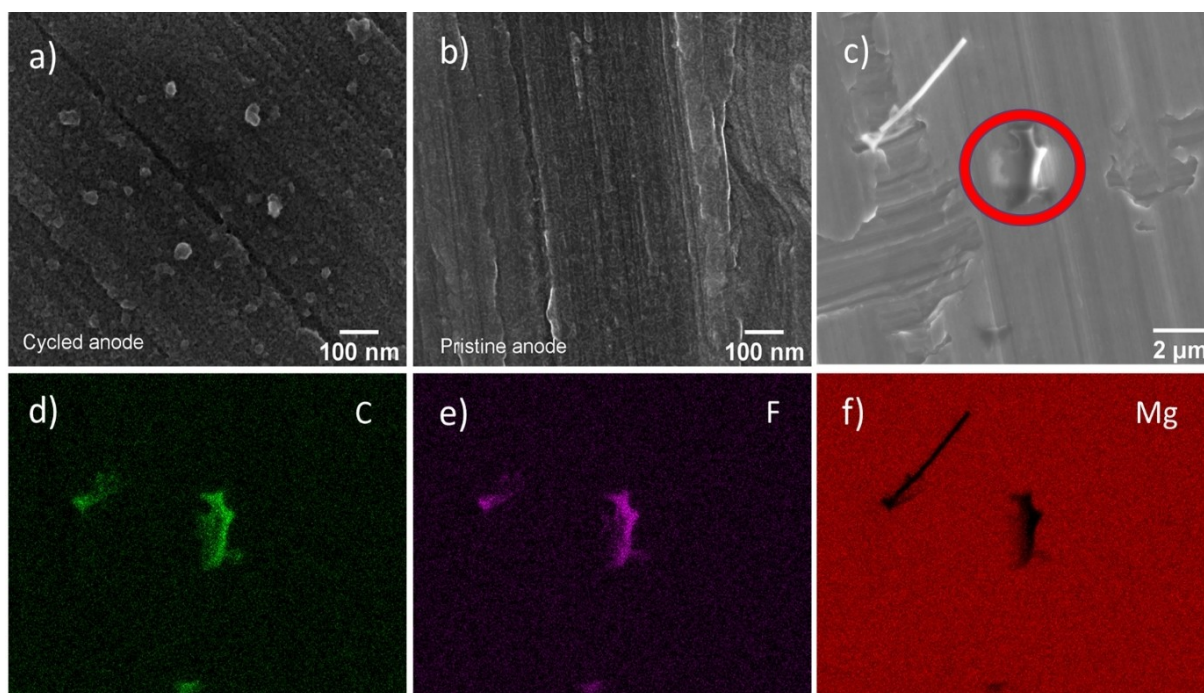European Chemical
Societies Publishing

Figure 6. a) Morphology of Mg anode surface after 20 cycles. b) Morphology of the pristine Mg anode. c) Prominent deposit on the cycled Mg anode. d–f) EDX mapping of the same site.

40 nm. Compared to the cycled Mg anode, no nano-spheres could be observed on the surface of the pristine Mg. The surface appeared to be even, dense and not porous. EDX measurement of the Mg anode (Figures S8) showed a strong magnesium signal along with small amounts of carbon and oxygen but no fluorine and boron. The absence of fluorine and boron signals hint that the interphase is a thin layer compared to the larger interaction volume from which the EDX signal is recorded. However, one site held a conspicuous deposition mounded on top of the surface as shown in Figure 6(c). The EDX mapping (Figures 6d–f) of this site showed a strong fluorine and carbon signal from the deposited species, but only a very weak magnesium signal within the deposit. This suggests that the deposition was most likely comprised of organofluoride species like $-CF_2$ and/or $-CF_3$ as indicated from the XPS measurements and not related to the MgF_2 based solid interphase. It must be mentioned that we did not find many sites with such depositions and much of the anode surface resembled the morphology shown in Figure 6(a).

Additionally, attempts were made to estimate the thickness of the solid interphase by analysing a cross-section through the surface of the cycled Mg anode. For that, cross-section was prepared and investigated via focused ion beam – scanning electron microscopy (FIB-SEM). The surface was first protected by depositing a Pt cover. Ga ion induced deposition of Pt (IBID) was avoided in the initial phase of Pt deposition in order to avoid the implantation of Ga ions in the uppermost parts of the surface. The occurrence of Ga in a thin layer of the sample lead to brighter grey values compared to the rest of the Mg anode in the secondary electron (SE) image due to a significant difference in atomic number between the two elements (Ga =

31, Mg = 12). A brighter layer caused by Ga ions can obscure a thin interphase and lead to misinterpretation. Ga implantation was avoided by two-step Pt deposition process. Initially Pt was deposited by electron beam induced deposition (EBID). In the second step, the thickness of the Pt cover was increased by IBID. Therefore, Ga implantation occurred within the Pt layer deposited by EBID only. The image of the prepared facet (Figure S9) of the cycled Mg anode showed a very thin layer. The layer was approximately 17 nm thick and compared reasonably well with the approximate thickness of the solid interphase estimated from XPS depth profile. However, it was not possible to further resolve this thin layer as the FIB-SEM was operated near its resolution limit. Hence, the results from the FIB-SEM were inconclusive when it came to analysing and identifying the solid interphase. High-resolution transmission electron microscopy (HR-TEM) will be required to further investigate such a thin solid interphase. Nonetheless, the SEM image of the surface of the cycled Mg anode does provide some evidence of the formation of a seemingly porous interphase.

Conclusion

In summary, we have presented results of a detailed study on the functioning and performance of a full-cell RMB, using a non-corrosive $Mg[B(hfip)_4]_2$/DME electrolyte, Mg metal anode and a layered TiS_2 cathode. This includes a study of the interphase formation at the anode-electrolyte interface in a full-cell RMB, which shows that the resulting solid interphase was approximately thicker than 10 nm and was primarily composed

of MgF_2, and boron-based species. Furthermore, post-cycle EIS measurements showed that the solid interphase formation led to a significant reduction in charge transfer resistance with cycling, demonstrating that the interphase layer was not passive, but actively improved reversible stripping and plating of Mg. On the other hand, the EIS findings during OCV condition showed increasing charge transfer resistance, indicating the formation of an ionically non-conducting adsorption layer. The corresponding full-cell measurements revealed a stable specific capacity of 50 mAh g^{-1} at room temperature over more than 100 cycles. Based on post-mortem analysis of the cathodes by XRD, we found that Mg^{2+} trapping in the TiS_2 lattice is a key hurdle for fully reversible charging/discharging. This conclusion was also supported by operando Raman measurements, while on the other hand it also showed a reasonable structural reversibility. Overall, we have tried to shed some light on the formation and functionality of the solid interphase layer at the anode-electrolyte interface in a full-cell RMB and at the same time also highlighted the challenges in the de-/insertion capability of the TiS_2 cathode, which requires further improvement to raise the overall performance of the RMB.

Experimental Section

Electrochemical measurement

Electrochemical measurements were carried out using two different configurations. Swagelok cell configuration was used to carry out galvanostatic measurements while PAT-Cell configuration from EL-CELL was used to conduct CV and EIS measurements. TiS_2 (99.9%, 200 mesh) was purchased from Aldrich and ball milled at 300 rpm with a milling time of 5 min followed by 10 min of rest, repeated for 16 times. The slurry was prepared by mixing 70% TiS_2 as the active material with 20% super P carbon black (Timcal) and 10% polyvinylidene difluoride (PVDF) from Solef in N-methyl-2-pyrrolidone (NMP). The slurry was then coated on 11.8 mm stainless steel current collectors. The cathodes were dried under vacuum at 80°C for 15 h. The tetrakis (hexafluoroisopropyloxy) borate ($Mg[B(hfip)_4]_2$) was synthesized by reacting $MgBH_4$ and hexafluoroisopropanol in DME in a one-pot reaction following our previous work.[15] The cells were assembled in an Ar-filled glovebox using 0.3 M $Mg[B(hfip)_4]_2$/DME as electrolyte, freshly polished Mg foil punched into 11 mm diameter disks as the anode and glass fibre GF/C separator. For the three-electrode configuration, we incorporated polished Mg foils of 16 mm diameter as the counter electrode while Mg ring was used as the reference (Mg_{ref}). VMP3 multichannel potentiostat from Bio-Logic was used for CV and EIS measurements and Arbin 2000T testing system was used for the galvanostatic measurements. The EIS measurements were conducted in the frequency range of 1 MHz–100 mHz. The impedance data was analysed by the Z fit function in the EC-Lab software. All electrochemical measurements were conducted at room temperature.

Material characterization

XRD: The XRD was carried out in a Stoe StadiP diffractometer with Mo radiation ($\lambda \sim 0.7092$ Å). The experiment was conducted in the Debye-Scherrer mode of operation with the samples sealed in glass ampules under inert atmosphere. The diffraction angles ranged

from 1° to 45° with a step size of 1° and a step time of 60 sec. All XRD measurements were carried out under Argon atmosphere.

FIB-SEM and EDX: FIB-SEM cross-sectioning and SEM imaging were done with a Helios Nanolab 600 (Thermo Fisher Scientific, USA). For EDX measurements, a SDD Apollo XV detector (EDAX, Germany) fitted to a Quanta 3D FEG (Thermo Fischer Scientific, USA) operated at 5 kV and 11 nA. The spectrum was measured for 50 live seconds (lvsec). For the mapping, 32 frames were measured with a dual time of 200 μs per pixel. For the cross-sections the platinum layer was deposited in a two-step process. First a Pt layer was deposited by electron beam induced deposition (EBID) using a voltage of 3 kV and a current of 2.8 nA. In a second step the thickness of the layer was enhanced by ion-beam induced deposition (IBID) operated at 30 kV and 46 pA to final thickness of about 700 nm. In both steps methylcyclopentadienyl trimethyl platinum ($C_9H_{16}Pt$) was used as precursor. Then a $14 \times 10 \times 3$ μm wedge was prepared at 30 kV and 2.8 nA as well as two trenches left and right to reduce shadow effects. The facet of the cross-section was polished at 30 kV and 0.28 nA. Imaging was done using the immersion mode and the through the lens detector (TLD) of the microscope using the secondary electron signal.

The SEM images of the pristine and ball milled TiS_2 powder were obtained using a Leo 1530 (Carl Zeiss Microscopy Deutschland Gmbh, Germany) at 15 kV. The EDX measurement of the pristine and cycled TiS_2 cathode was done with EDX detector X-maxN from Oxford instruments. The TiS_2 samples were prepared on carbon tape and were gold sputtered.

Operando Raman: Raman spectra were collected at room temperature in the spectral range 100–700 cm^{-1} by using an inVia™ confocal Raman microscope (RENISHAW) with an excitation laser of 633 nm wavelength. To avoid sample over-heating, the nominal laser power was filtered down to $\sim$2.5 mW. The slit opening of the confocal system was fixed at 65 mm and centred at 1867 μm. For the collection of spectra, backscattering geometry with a $20 \times$ magnification objective was applied. To increase the signal-to noise ratio, each spectrum was averaged over 5 accumulations for 5 sec each.

The probed sample spot was continuously focused during the experiment using an autofocus function. Analysis of the Raman data was conducted using the inVia WiRE 4.4 Software. Operando Raman measurements were conducted using an ECC Opto-Std (EL-CELL GmbH) electrochemical cell connected with the Raman microscope. In the sample preparation, a thick slurry containing 90 wt% TiS_2 as the active material, 5 wt% conductive carbon and 5 wt% polyvinylidene difluoride (PVDF) was deposited onto a Inconel 625 current collector disc (16 mm) with a 1 mm hole in the middle. The resulting electrodes were dried for 12 h in an oven at a temperature of 100°C. The operando cell was assembled in an argon filled glove box (MBRAUN) with TiS_2 as positive electrode, polished Mg metal disc as the anode and a borosilicate glass fibre soaked with 0.3 M $Mg[B(hfip)_4]_2$/DME as electrolyte. The cathode side of the cell was sealed with a thin optical glass window (0.15 mm) and was made air-tight with a rubber seal. The battery tester used was an Interface 1000™ Potentiostat/Galvanostat/ZRA (Gamry Instruments, Inc.) workstation with Gamry Echem Analyst software.

FTIR: FTIR experiments were performed using FTIR spectrometer (Spectrum Two, PerkinElmer) in the spectral range of 500–2000 cm^{-1}

XPS: The chemical state of the surface of an electrode which was subjected to 20 electrochemical cycles was determined by XPS measurements using monochromatized Al K_α (1486.6 eV) radiation (PHI 5800 MultiTechnique ESCA System, Physical Electronics). The

measurements were done with a detection angle of 45°, using pass energies at the analyzer of 93.9 eV and 29.35 eV for survey and detail spectra, respectively. The sample was neutralized with electrons from a flood gun to compensate for the charging effects at the surface. Spectra were recorded at the topmost surface and after repeated Ar^+ ion sputtering (5 kV, 1 μA) for 3 and 7 min (leading to a total time of 10 min). The nominal sputter rate is ~1 nm min^{-1}, i.e., 3 and 10 nm of the surface layer were removed. It is important to clarify that the nominal sputtering rate is provided by the manufacturer and is only an approximation. Sputtering rate depends on the yield which in turn is a function of angle of impact of the impinging ions, substrate material, energy and type of impinging ions. Hence from the manufacturer provided nominal sputtering rate we do not get an accurate estimate of the depth of layer removed from the surface. For binding energy calibration, the main C 1s peak was set to 284.8 eV. Peak fitting was done with Casa XPS using Shirley-type backgrounds and Gaussian-Lorentzian peak profiles.

Acknowledgements

Conflict of Interest

The authors declare no conflict of interest.

[1] D. Aurbach, Y. Cohen, M. Moshkovich, *Electrochem. Solid-State Lett.* **2001**, *4*, A113.
[2] M. Jäckle, A. Groß, *J. Chem. Phys.* **2014**, *141*, 174710.
[3] P. Canepa, G. Sai Gautam, D. C. Hannah, R. Malik, M. Liu, K. G. Gallagher, K. A. Persson, G. Ceder, *Chem. Rev.* **2017**, *117*, 4287–4341.
[4] D. Aurbach, Z. Lu, A. Schechter, Y. Gofer, H. Gizbar, R. Turgeman, Y. Cohen, M. Moshkovich, E. Levi, *Nature* **2000**, *407*, 724–727.
[5] Z. Zhao-Karger, R. Liu, W. Dai, Z. Li, T. Diemant, B. P. Vinayan, C. Bonatto Minella, X. Yu, A. Manthiram, R. J. Behm, M. Ruben, M. Fichtner, *ACS Energy Lett.* **2018**, *3*, 2005–2013.
[6] P. Wang, J. Trück, S. Niesen, J. Kappler, K. Küster, U. Starke, F. Ziegler, A. Hintennach, M. R. Buchmeiser, *Batteries & Supercaps* **2020**, *3*, 1239–1247; Supercaps **2020**, 3, 1239–1247.
[7] P. Wang, K. Küster, U. Starke, C. Liang, R. Niewa, M. R. Buchmeiser, *J. Power Sources* **2021**, *515*, 230604.
[8] D. Aurbach, Y. Gofer, A. Schechter, O. Chusid, H. Gizbar, Y. Cohen, M. Moshkovich, R. Turgeman, *J. Power Sources* **2001**, *97–98*, 269–273.
[9] Z. Lu, A. Schechter, M. Moshkovich, D. Aurbach, *J. Electroanal. Chem.* **1999**, *466*, 203–217.
[10] R. Attias, M. Salama, B. Hirsch, Y. Goffer, D. Aurbach, *Joule* **2019**, *3*, 27–52.
[11] D. Aurbach, H. Gizbar, A. Schechter, O. Chusid, H. E. Gottlieb, Y. Gofer, I. Goldberg, *J. Electrochem. Soc.* **2002**, *149*, A115.
[12] R. Mohtadi, M. Matsui, T. S. Arthur, S.-J. Hwang, *Angew. Chem. Int. Ed.* **2012**, *51*, 9780–9783; *Angew. Chem.* **2012**, *124*, 9918–9921.
[13] S.-Y. Ha, Y.-W. Lee, S. W. Woo, B. Koo, J.-S. Kim, J. Cho, K. T. Lee, N.-S. Choi, *ACS Appl. Mater. Interfaces* **2014**, *6*, 4063–4073.
[14] O. Tutusaus, R. Mohtadi, T. S. Arthur, F. Mizuno, E. G. Nelson, Y. V. Sevryugina, *Angew. Chem. Int. Ed.* **2015**, *54*, 7900–7904; *Angew. Chem.* **2015**, *127*, 8011–8015.
[15] Z. Zhao-Karger, M. E. Gil Bardaji, O. Fuhr, M. Fichtner, *J. Mater. Chem. A* **2017**, *5*, 10815–10820.
[16] Z. Zhang, Z. Cui, L. Qiao, J. Guan, H. Xu, X. Wang, P. Hu, H. Du, S. Li, X. Zhou, S. Dong, Z. Liu, G. Cui, L. Chen, *Adv. Energy Mater.* **2017**, *7*, 1602055.
[17] Z. Ma, D. R. MacFarlane, M. Kar, *Batteries & Supercaps* **2019**, *2*, 115–127; Supercaps **2019**, 2, 115–127.
[18] J. Muldoon, C. B. Bucur, A. G. Oliver, J. Zajicek, G. D. Allred, W. C. Boggess, *Energy Environ. Sci.* **2013**, *6*, 482–487.
[19] Z. Ma, M. Kar, C. Xiao, M. Forsyth, D. R. MacFarlane, *Electrochem. Commun.* **2017**, *78*, 29–32.
[20] N. Sa, B. Pan, A. Saha-Shah, A. A. Hubaud, J. T. Vaughey, L. A. Baker, C. Liao, A. K. Burrell, *ACS Appl. Mater. Interfaces* **2016**, *8*, 16002–16008.
[21] F. Mizuno, N. Singh, T. S. Arthur, P. T. Fanson, M. Ramanathan, A. Benmayza, J. Prakash, Y.-S. Liu, P.-A. Glans, J. Guo, *Front. Energy Res.* **2014**, *2*.
[22] O. Tutusaus, R. Mohtadi, N. Singh, T. S. Arthur, F. Mizuno, *ACS Energy Lett.* **2017**, *2*, 224–229.
[23] T. S. Arthur, P.-A. Glans, N. Singh, O. Tutusaus, K. Nie, Y.-S. Liu, F. Mizuno, J. Guo, D. H. Alsem, N. J. Salmon, R. Mohtadi, *Chem. Mater.* **2017**, *29*, 7183–7188.
[24] R. Mohtadi, O. Tutusaus, T. S. Arthur, Z. Zhao-Karger, M. Fichtner, *Joule* **2021**, *5*, 581–617.
[25] R. Jay, A. W. Tomich, J. Zhang, Y. Zhao, A. De Gorostiza, V. Lavallo, J. Guo, *ACS Appl. Mater. Interfaces* **2019**, *11*, 11414–11420.
[26] M. S. Whittingham, *Science* **1976**, *192*, 1126–1127.
[27] E. Levi, Y. Gofer, D. Aurbach, *Chem. Mater.* **2010**, *22*, 860–868.
[28] L. E. Blanc, X. Sun, A. Shyamsunder, V. Duffort, L. F. Nazar, *Small Methods* **2020**, *4*, 2000029.
[29] X. Sun, P. Bonnick, L. F. Nazar, *ACS Energy Lett.* **2016**, *1*, 297–301.
[30] D. S. Tchitchekova, A. Ponrouch, R. Verrelli, T. Broux, C. Frontera, A. Sorrentino, F. Bardé, N. Biskup, M. E. Arroyo-de Dompablo, M. R. Palacín, *Chem. Mater.* **2018**, *30*, 847–856.
[31] E. Orazem, B. Tribollet, *Electrochem. Impedance Spectrosc.* **2008**, 153–162.
[32] E. Peled, D. Golodnitsky, G. Ardel, *J. Electrochem. Soc.* **1997**, *144*, L208–L210.
[33] D. A. Long, *J. Raman Spectrosc.* **2004**, *35*, 905–905.
[34] V. Bhaghavathi Parambath, Z. Zhao-Karger, T. Diemant, M. Jäckle, Z. Li, T. Scherer, A. Gross, R. J. Behm, M. Fichtner, *J. Mater. Chem. A* **2020**, *8*, 22998–23010.
[35] B. Li, R. Masse, C. Liu, Y. Hu, W. Li, G. Zhang, G. Cao, *Energy Storage Mater.* **2019**, *22*, 96–104.
[36] Z. Li, O. Fuhr, M. Fichtner, Z. Zhao-Karger, *Energy Environ. Sci.* **2019**, *12*, 3496–3501.
[37] Z. Li, T. Diemant, Z. Meng, Y. Xiu, A. Reupert, L. Wang, M. Fichtner, Z. Zhao-Karger, *ACS Appl. Mater. Interfaces* **2021**, *13*, 33123–33132.

RESEARCH ARTICLE

Rechargeable magnesium batteries: The interaction between non-noble Mg anode and a non-corrosive fluorinated alkoxyborate-based electrolyte $Mg[B(hfip)_4]_2$/DME leads to the decomposition of the $[B(hfip)]^-$ at the Mg anode on cycling, forming a MgF_2 and boron-based thin solid interphase which sustains reversible plating/stripping in a full-cell magnesium battery.
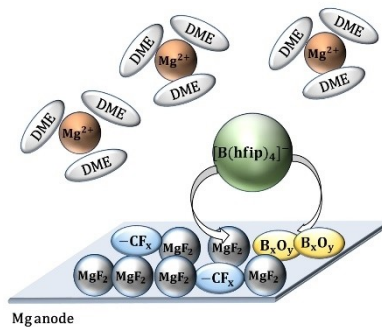
A. Roy, Dr. V. Bhagavathi Parambath, Dr. T. Diemant, Dr. G. Neusser, Prof. C. Kranz, Prof. R. J. Behm, Dr. Z. Li*, Dr. Z. Zhao-Karger, Prof. M. Fichtner

1 – 10

Investigation of the Anode-Electrolyte Interface in a Magnesium Full-Cell with Fluorinated Alkoxyborate-Based Electrolyte